ACS OMEGA

Open Access

http://pubs.acs.org/journal/acsodf

Article

All-Solution-Processed IGZO Optoelectronic Synaptic Transistor with Dual-Mode Operation toward Artificial Vision Applications

Haonan Xu,[‡] Lilan Zou,[‡] Junru An, and Shiwei Lin*

Cite This: *ACS Omega* 2025, 10, 16884−16891

Read Online

ACCESS | Metrics & More | Article Recommendations | Supporting Information

ABSTRACT: Realizing the dual-mode electric and optical synaptic plasticity within one neuromorphic device is impressive for the construction of a compact artificial visual system. Here, we proposed indium gallium zinc oxide (IGZO) photoelectric synaptic transistors utilizing all-solid-state electrolytes (Li-doped ZrO_2) as gate dielectric layers. The device was fabricated by using a facile and cost-effective all-solution method. The synaptic transistor exhibited dual-mode electric and optical synaptic plasticity. Meanwhile, the tunable conductance is achieved through electric potentiation and depression processes, demonstrating the potential for realizing neuromorphic computing. Based on this, a simulated convolutional neural network was designed to realize handwriting digit recognition, achieving an accuracy of 96.8%. Additionally, sophisticated neuromorphic applications such as logic operations, Pavlov's classical experiment, and pupillary reflex simulation were successfully realized. Therefore, the designed transistor demonstrates significant potential for future applications in artificial vision.

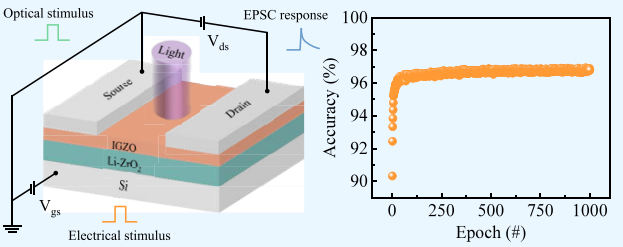

1. INTRODUCTION

The human visual system allows us to access over 80% of external information through ocular perception.[1] Furthermore, it concurrently executes sensing, memory, and processing tasks, thereby demonstrating its inherent advantage in energy efficiency.[2] An artificial vision system (AVS) is essential for enabling intelligent applications, such as automatic drives, smart robots, and brain−computer interfaces.[3−5] Nonetheless, traditional AVS architectures face challenges including data access latency and higher power consumption, which stem from the separation of functional units including image sensors, memory, and processors.[6−8] Drawing inspiration from the human visual system, researchers have focused on developing biomimetic optoelectronic neuromorphic devices. The photoelectric memristors and transistors, which exhibit the potential for in-sensor computing, are crucial components for developing an energy-efficient AVS.[9] The three-terminal synaptic transistors have significant advantages of good stability, clear operation mechanism, and gate-tunable plasticity, rendering them a promising candidate for future AVS applications.[10−12]

It is worth mentioning that realizing the dual-mode electric and optical synaptic plasticity within one neuromorphic device is impressive for constructing a complete AVS. This enhances energy efficiency and mitigates fabrication complexity arising from process incompatibility.[13,14] However, the challenge persists in three-terminal transistors for achieving electric synaptic plasticity utilizing conventional oxide dielectric layers.[15] The electrochemical synaptic transistor, which utilizes an electrolyte as the gate dielectric, has emerged as a promising candidate. The ion liquid, polymer, or gel electrolytes exhibit significant limitations toward future high-integration density applications. For this reason, utilizing all-solid-state electrolytes as gate dielectric layers to achieve electric plasticity is highly desirable and has garnered considerable attention.[16,17] Furthermore, the electric synaptic model is inadequate for accurately simulating the complex functions of the human visual system. The synaptic transistor that integrates both electric and optical synaptic plasticity for constructing a comprehensive AVS is urgently needed. Indium gallium zinc oxide (IGZO) is a wide bandgap semiconductor, which exhibits excellent photoresponse to UV light illumination.[18−20] Meanwhile, the persistent photoconductivity (PPC) in the IGZO layer enables the simulation of diverse optical synaptic plasticity.[21]

In this work, we propose a synaptic transistor that employs Li-doped ZrO_2 (Li-ZrO_2) as the gate dielectric layer and IGZO as the channel material. The IGZO/Li-ZrO_2 film was fabricated via an all-solution process, which offers the advantages of straightforward processing, low fabrication costs, and scalability for large-area preparation. The designed transistor exhibits dual-mode electric and optical synaptic plasticity, enabling neuromorphic computing and sensing on a single device. In addition, digital logic functions (AND and OR

Received: February 3, 2025
Revised: April 4, 2025
Accepted: April 9, 2025
Published: April 18, 2025

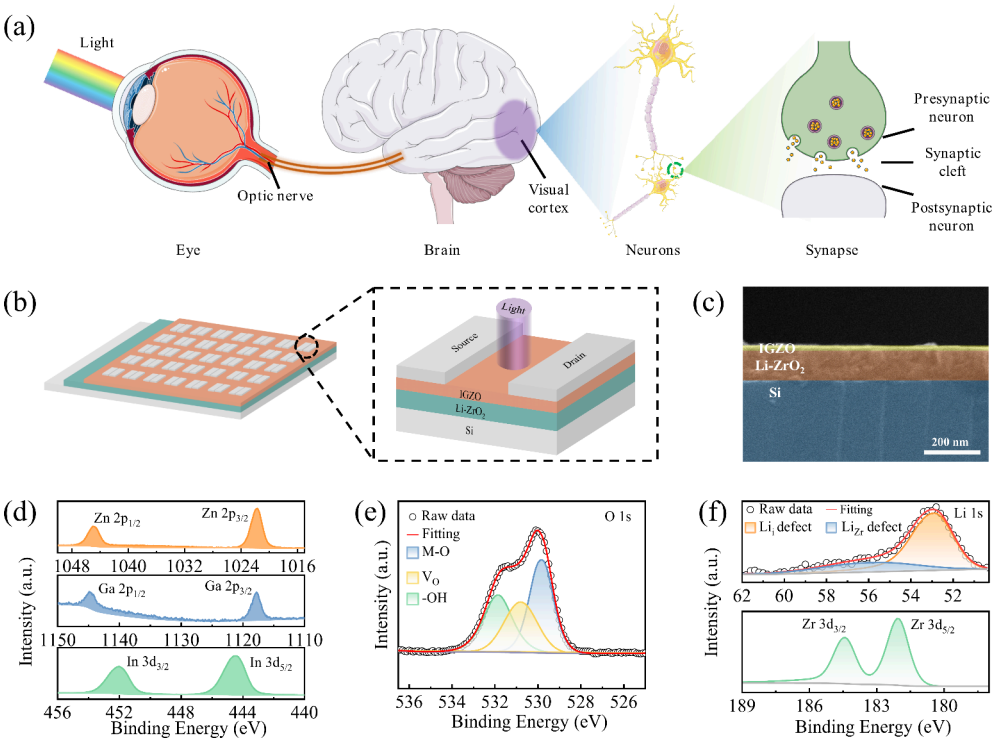

Figure 1. Schematic diagrams of the (a) biological visual nervous system and the (b) device structure. (c) SEM image of the IGZO/Li-ZrO_2/Si device. XPS spectra of (d) In 3d, Ga 2p, Zn 2p, and (e) O 1s in the IGZO thin film. (f) XPS spectra of Li 1s and Zr 3d in the Li-ZrO_2 thin film.

gate), Pavlov's experiment, and gate-tunable plasticity were realized in our device. Our work offers a valuable method for the development of dual-mode optoelectronic synaptic transistors for artificial vision applications.

2. EXPERIMENTAL SECTION

2.1. Materials. To prepare the Li-doped ZrO_2 film, the precursor solution was synthesized using $Zr(NO_3)_4{\cdot}5H_2O$ and $LiClO_4$ as raw materials, with 2-methoxyethanol (2-ME) as the cosolvent. The mixture containing 10% Li^+ (0.1 M) was stirred for 12 h to obtain a transparent precursor solution. The IGZO precursor solution with a molar ratio of 6:3:1 was prepared by dissolving $In(NO_3)_3{\cdot}xH_2O$, $Ga(NO_3)_3{\cdot}xH_2O$, and $Zn(NO_3)_2{\cdot}6H_2O$ in 2-ME, followed by stirring for 12 h to obtain a clear and transparent solution.

2.2. Device Fabrication. The Li-doped ZrO_2 precursor solution was spin-coated onto a cleaned silicon substrate at 3000 rpm for 20 s, followed by annealing at 600 °C for 2 h with a controlled heating rate of 5 °C/min. Subsequently, the IGZO precursor solution was deposited via spin coating at 3000 rpm for 30 s onto the Li-doped ZrO_2 dielectric layer, followed by postdeposition annealing at 400 °C for 1 h using the same controlled ramp rate of 5 °C/min. Finally, the transistor was fabricated by depositing aluminum onto the IGZO film as the source and drain electrodes through thermal evaporation. The channel dimensions have a length of 70 μm and a width of 2000 μm.

2.3. Characterization and Testing of Devices. The cross-sectional images were characterized using scanning electron microscopy (SEM, Verios G4 US, Thermo Fisher Scientific, USA). The composition of the thin films was determined by using X-ray photoelectron spectroscopy (XPS, Thermo Escalab 250XI, Thermo Fisher Scientific, USA). Electrical characterization and optoelectronic synaptic plasticity assessment of the optoelectronic synaptic transistor were conducted by utilizing a Keithley 2614B semiconductor parameter analyzer in conjunction with a probe station system. Illumination was provided by LEDs with varying wavelengths and adjustable power levels, as depicted in Figure S1.

3. RESULTS AND DISCUSSION

The human visual nervous system consists of the retina, optic nerve, and visual cortex, as illustrated in Figure 1a. Images are projected onto the retina and converted into electrical signals by the photoreceptor cells. Then, the visual signals are transmitted to the visual center via the optic nerve for high-level processing.[22−24] Synapses are the fundamental units for information transmission and processing within the visual system, encompassing presynaptic neurons, postsynaptic neurons, and cleft.[25] The synaptic weight represents the connection strength between presynaptic and postsynaptic neurons, which can be adjusted through input signals, a process known as synaptic plasticity.[26] Inspired by the human visual system, an artificial vision device-based three-terminal transistor was proposed here. As shown in Figure 1b, the transistor functions as a three-terminal synapse, where the gate serves as a weight neuromodulator and electric input as a presynaptic neuron.

The microstructure of the films was characterized by SEM, as depicted in Figure 1c. The IGZO layer has a thickness of about 20 nm, while the Li-ZrO_2 layer exhibits a thickness of 100 nm. A cross-sectional SEM image of the individual Li-ZrO_2 layer is shown in the Supporting Information, Figure S2. The chemical composition of the IGZO and Li-ZrO_2 layers was investigated using XPS. As illustrated in Figure 1d, the XPS spectrum of the Zn 2p orbit exhibits two doublet peaks at 1044.9 and 1021.8 eV, corresponding to Zn $2p_{1/2}$ and Zn $2p_{3/2}$, respectively. The two peaks of the Ga 2p orbit located at

https://doi.org/10.1021/acsomega.5c01052
ACS Omega 2025, 10, 16884−16891

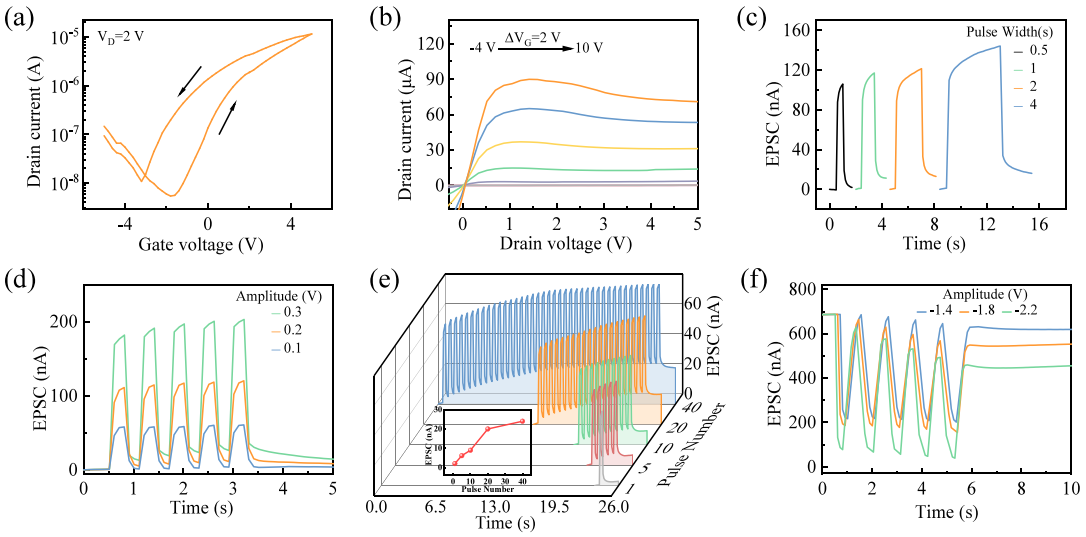

Figure 2. (a) Transfer and (b)output curves of the transistor. (c) Voltage pulse width-dependent plasticity. (d) Pulse amplitude-dependent plasticity. (e) Pulse number-dependent plasticity. The inset exhibits the EPSC as a function of pulse number. (f) Transition from STD to LTD.

1144.8 and 1117.8 eV correspond to Ga $2p_{1/2}$ and Ga $2p_{3/2}$, respectively. Similarly, the two peaks of the In 3d orbit observed at 452.1 and 444.5 eV are attributed to In $3d_{3/2}$ and In $3d_{5/2}$, respectively. The XPS peak of O 1s of IGZO was fitted into three peaks at 529.9, 530.8, and 531.9 eV, corresponding to metal−oxygen (M−O) bonding, oxygen vacancy (V_O), and chemisorbed hydroxide (−OH) bonding, respectively.[27] The chemical composition analysis confirmed the successful preparation of the IGZO film. Figure 1f shows the Li 1s and Zr 3d orbitals of the Li-ZrO_2 layer. The two peaks at 182.1 and 184.4 eV correspond to Zr $3d_{5/2}$ and Zr $3d_{3/2}$, respectively.[28] The fitting results of the Li 1s peaks reveal the presence of two distinct doping states within the Li-ZrO_2 layer. The peak at 55.4 eV is attributed to Li_{Zn}-O bonds associated with Li_{Zn} defects, while the peak at 52.9 eV is ascribed to interstitial Li atoms corresponding to Li_i defects.[29] Thus, the channel layer and solid electrolyte have been successfully fabricated by using the all-solution method.

Figure 2a shows the transfer curve of the transistor with a counterclockwise hysteresis window, which is imperative for simulating electric synaptic plasticity. The transfer curve for the device without Li^+ doping in the ZrO_2 film, as shown in Figure S3, exhibits a notably small counterclockwise hysteresis window. Therefore, the Li^+ implantation is responsible for this hysteresis effect, which can be explained by the Li^+ electrochemical doping/dedoping model, as shown in Figure S4. The Li^+ ions accumulate at the interface of Li-ZrO_2/IGZO when a positive gate voltage is applied. Meanwhile, the electrons attracted to the interface contribute to the channel conductance. The conductance cannot return to its initial state due to the accumulation of electrons through electrostatic attraction, resulting from Li^+ electrochemical doping at the interface.[30] A sufficiently large negative gate voltage is required to drag Li^+ ions from the interface, reducing the channel conductance.[31,32] Therefore, the doping and dedoping mechanisms of conductive ions not only account for the hysteresis window observed in electrolyte-gated synaptic transistors but also fundamentally govern their electrical synaptic plasticity. Consequently, the quality of electrical synaptic plasticity can be indirectly assessed through the hysteresis window manifested in the transfer characteristics of the transistor.[31] The optimization of the fabrication conditions for Li-ZrO_2 is illustrated in Figure S5. The transistor based on Li-ZrO_2 annealed at 600 °C exhibits the most significant hysteresis window and was therefore chosen for our subsequent investigation. Figure 2b illustrates the output characteristics of the designed transistor in response to varying gate voltages ranging from −4 to 10 V. In biological synapses, the release of neurotransmitters, triggered by the action of a presynaptic neuron, results in either excitatory postsynaptic currents (EPSC) or inhibitory postsynaptic currents (IPSC) in the postsynaptic neuron. This results in strengthened connections between two neurons over an extended period of time, a phenomenon known as long-term potentiation (LTP). In contrast, short-term plasticity (STP) leads to transient synaptic weight enhancement.[33] The designed transistor can simulate a biological synapse to achieve diverse synaptic functions. Figure 2c demonstrates voltage pulse width-dependent plasticity, where the gate and drain electrodes are presynaptic and postsynaptic neurons, respectively, and the IGZO layer is the synaptic cleft. The electric spike input from the gate terminal results in increased conductance. A larger voltage amplitude or repeating stimuli leads to a larger EPSC and the transition from STP to LTP, as shown in Figure 2d,e. It is attributed to the fact that the prolonged duration of the electric pulse facilitates a greater accumulation of Li^+ ions at the Li-ZrO_2/IGZO interface, thereby leading to an increased EPSC. The electric depression process and IPSC were observed when a negative gate voltage was applied, as illustrated in Figure 2f. The transition from short-term depression (STD) to long-term depression (LTD) was achieved as the negative voltage amplitude increased from −1.4 to −2.2 V. The simulation of electric synaptic plasticity underscores its significant potential in facilitating neural network computing.

To further demonstrate the potential of the transistor for neuromorphic computing, tunable conductance was achieved through electric potentiation (V_G pulses: 0.25 V, 100 ms) and a depression process (V_G pulses: −0.2 V, 100 ms), as illustrated in Figure 3a. The potentiation and depression processes can also be realized by integrating UV light pulses with negative gate voltage pulses, exhibiting good linearity, as

https://doi.org/10.1021/acsomega.5c01052
ACS Omega 2025, 10, 16884−16891

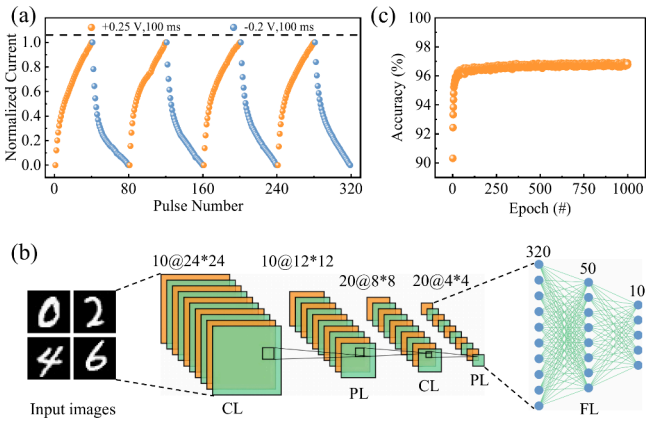

Figure 3. (a) Repeating potentiation and depression behavior. (b) Schematic diagram of a six-layered convolutional neural network (CNN). (c) Recognition accuracy for handwritten digit images based on experimental potentiation and the depression process.

shown in Figure S6. The repetitive potentiation and depression processes demonstrate the stability and reliability of the neuromorphic device. A six-layer convolutional neural network (CNN) was specifically designed for the classification of 28 × 28 pixels images from the Modified National Institute of Standards and Technology (MNIST) data set. It comprises two convolutional layers (CL), two max-pooling layers (PL), and two fully connected layers (FL). The model modifies the weights of the fully connected layers within the network in accordance with actual measurement results obtained from devices. As depicted in Figure 3b, the neural network processes a 28 × 28-pixel handwritten digit image as its input. The initial processing stage generates feature maps of a size of 24 × 24 pixels with 10 channels through convolution operations. Subsequent pooling operations reduce the feature dimensions to 12 × 12 × 10 while preserving channel depth. In the secondary feature extraction phase, enhanced convolutional processing yields representations of a size of 8 × 8 pixels across 20 channels, followed by further dimensionality reduction to 4 × 4 × 20 through additional pooling operations. Feature maps generated from the second convolutional and pooling layers are input into the fully connected layer. This initial fully connected layer comprises a weight matrix with dimensions of 320 × 50. The output from this layer is then transmitted to a subsequent fully connected layer, which features a weight matrix of 50 × 10, representing 50 input nodes and 10 output nodes corresponding to digit classes ranging from 0 to 9. This transformation maps high-dimensional feature vectors to categorical probability distributions. The final output layer consisted of 10 neurons arranged in a fully connected configuration. A Softmax activation function is employed to convert the network outputs into normalized class probabilities, ultimately determining the classification results for the input images. Trainable parameters, including convolutional kernel coefficients and fully connected weight matrices, can be

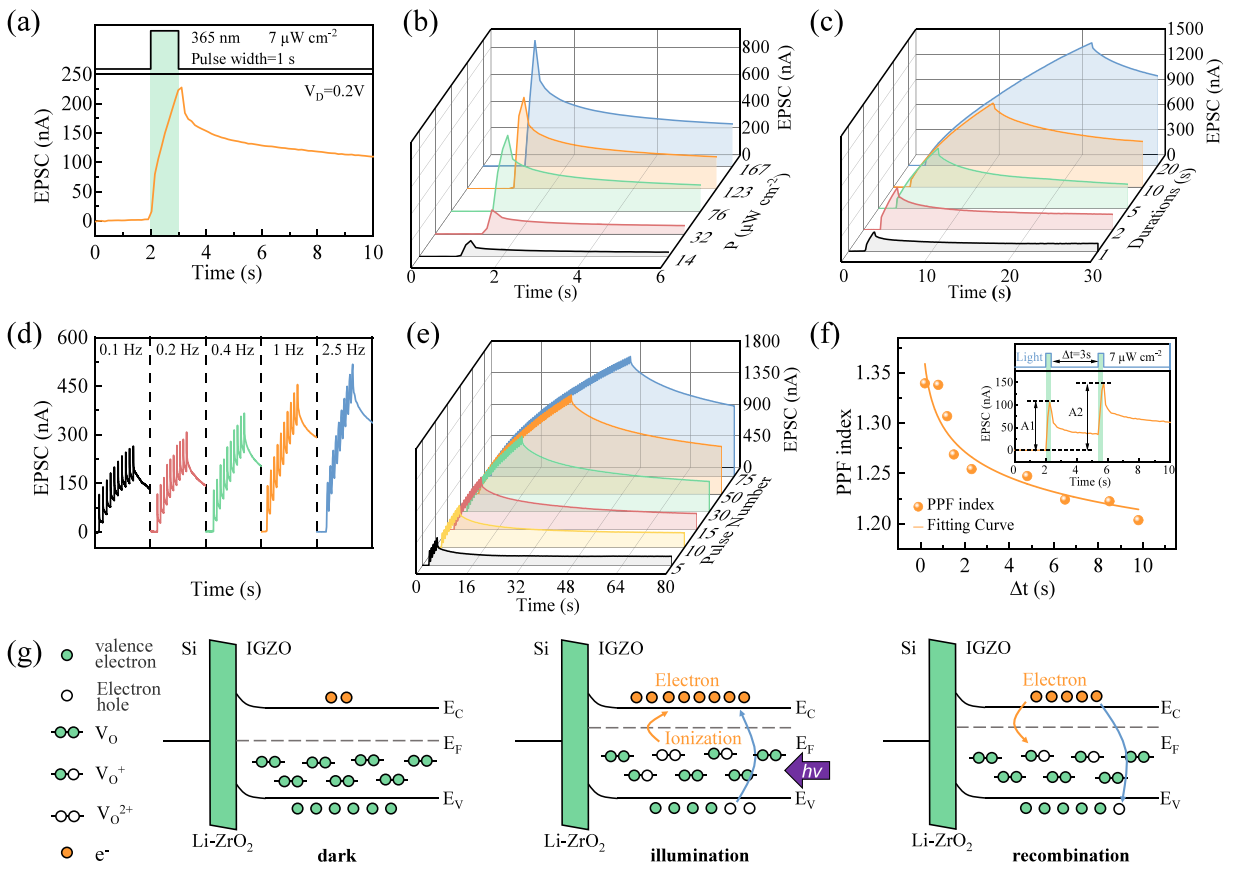

Figure 4. (a) EPSC of a synaptic transistor triggered by one optical spike. (b) PIDP (V_D = 0.2 V, pulse width = 200 ms). (c) PWDP (V_D = 0.2 V, pulse power = 7 μW cm^{-2}). (d) PFDP (V_D = 0.2 V, pulse width = 200 ms, pulse power = 7 μW cm^{-2}). (e) PNDP (V_D = 0.2 V, pulse width = 200 ms, pulse power = 7 μW cm^{-2}). (f) PPF index as a function of pulse intervals (Δt). The inset shows a typical PPF behavior. (g) Schematic diagram of the photoresponse mechanism in an IGZO-based transistor.

https://doi.org/10.1021/acsomega.5c01052
ACS Omega 2025, 10, 16884−16891

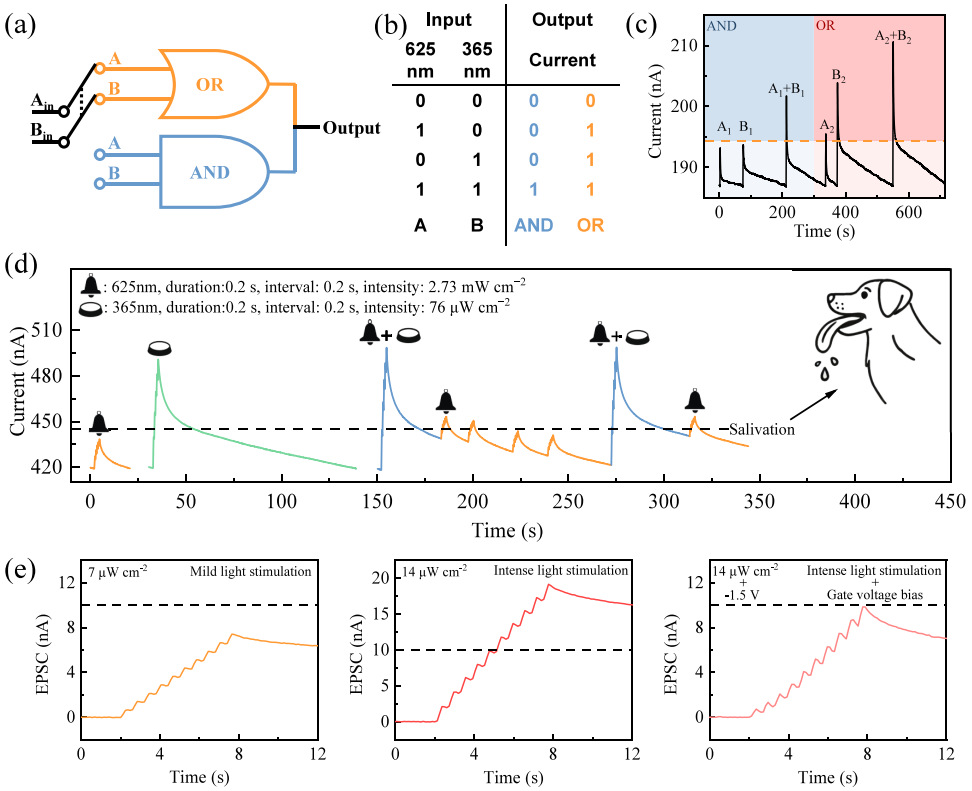

Figure 5. (a) Schematic diagrams of AND gate and OR gate. (b) Truth table of the optical logic AND gate and OR gate. (c) OR and AND logical functions utilizing 625 and 365 nm optical pulses as inputs A and B, respectively. (d) Demonstration of Pavlov's classical conditioned reflex. (e) Simulating pupillary response of the human visual system in response to light stimuli with different intensities.

derived from the conductance values of synaptic transistors through their potentiation and depression curve characteristics.[34] For the classification of handwritten digits, the CNN simulation demonstrates a high accuracy of 96.8% based on experimentally measured potentiation and depression characteristics, as demonstrated in Figure 3c.

Optical synaptic plasticity plays a crucial role in neuromorphic sensing. The neuromorphic vision device integrates the sensing and preprocessing functions, thus exhibiting more energy efficiency. Here, the optical synaptic plasticity of the designed transistor in response to 365 nm light illumination has been investigated. The photocurrent was monitored at V_{DS} = 0.2 V. The device exhibits obvious EPSC and PPC effects upon one light pulse (7 μW/cm^2, duration: 1 s), as demonstrated in Figure 4a. The energy consumption for a single optical synaptic activity is shown in Figure S7, exhibiting a low energy consumption of 1.3 pJ. The light dose-dependent synaptic plasticities, including the pulse intensity-dependent plasticity (PIDP), pulse width-dependent plasticity (PWDP), pulse frequency-dependent plasticity (PFDP), and pulse number-dependent plasticity (PNDP), have been investigated, as demonstrated in Figure 4b−e, respectively. A larger EPSC and transition from STP to LTP were observed as the light dose (intensity, duration, frequency, and number) increased, which was ascribed to the greater influx of photons absorbed in the IGZO layer. It generates a large number of electrons in the channel and triggers more pronounced EPSC and PPC effects. Paired-pulse facilitation (PPF) is a prototypical form of STP, characterized by an enhanced EPSC in response to two consecutive stimuli. The inset of Figure 4f illustrates the EPSC generated by a pair of optical pulses (365 nm, duration: 200 ms, interval: 3 s). The PPF index is defined as PPF = 100% × A_2/A_1, where A_1 and A_2 represent the amplitudes of the EPSC induced by the first and second optical pulse, respectively.[35,36] The PPF index as a function of intervals is shown in Figure 4f, and the PPF index decreases as the interval increases. The decay behavior of the PPF index can be fitted by using a double-exponential function, which is consistent with the trend observed in biological synapses. The PPC effect can be explained by the energy band diagram. The original IGZO film has a significant number of V_O during the fabrication. Upon exposure to UV light, oxygen vacancies are ionized, generating electrons ($V_O \rightarrow V_O^+ + e^-$ or $V_O \rightarrow V_O^{2+} + 2e^-$), which increases the conductivity of the IGZO channel.[37] The excited electrons are unable to directly recombine with ionized V_O^{2+} or V_O^+ due to the energy barrier, leading to the PPC effect, as demonstrated in Figure 4g.[38,39] The designed transistor can simulate diverse synaptic behaviors, exhibiting the potential for neuromorphic sensing, akin to the human retina.

In biological neural systems, a neuron can receive and integrate signals from multiple neurons to perform complex tasks such as logic computations.[40−42] As shown in Figure 5a, the logic functions, including AND and OR gates, can be achieved by an all-optical approach using 625 and 365 nm light as inputs A and B, respectively. Figure 5b,c presents the corresponding truth table and operation process, where the input signals "1" and "0" indicate the presence or absence of an optical signal, respectively. When the photocurrent induced by the input signals exceeds the threshold value (set at 194 nA), the output is recorded as "1"; otherwise, it is recorded as "0". For the simulation, the AND gate was achieved using input A_1 (625 nm, 2.27 mW/cm^2) and input B_1 (365 nm, 7 μW/cm^2).

https://doi.org/10.1021/acsomega.5c01052
ACS Omega 2025, 10, 16884−16891

Only when both inputs A_2 and B_2 were applied to the device synchronously could the threshold value be achieved. For the OR gate, input A (625 nm, 2.73 mW/cm^2) or B (365 nm, 14 μW/cm^2) can reach the threshold. Classical conditioning, also referred to as Pavlov's conditioning, is an associational learning process, in which an initially neutral stimulus is repeatedly paired with an unconditioned stimulus, thereby establishing connections between associations and inducing behavioral modifications.[43−45] Pavlov's experiment was simulated by the designed transistor using 625 nm (2.73 mW/cm^2) light pulses as the neutral stimulus (bell ring), with 365 nm (76 μW/cm^2) light pulses as the unconditioned stimulus (food). Prior to the establishment of associative learning, the bell ring alone does not elicit salivation (a threshold value of 448 nA). The training process involves simultaneously applying both the bell ring and food stimuli to establish a connection between them. Then, the bell ring stimulus alone can induce salivation. Over time, the neutral stimulus failed to induce salivation. It is essential to re-establish the connections by repeating the training process. The logic functions and Pavlov's experiment have been successfully emulated using an all-optical approach, demonstrating significant potential for realizing complex neuromorphic tasks. The mechanism of sub-bandgap photon-induced photoresponse in IGZO, involving defect-mediated excitation processes, is illustrated in the Supporting Information, Figure S8.

The human pupil can dynamically adjust the luminous flux in response to external light intensities, thereby mitigating potential damage to the retina from excessive light exposure.[46,47] The three-terminal transistor, with the gate serving as the modulatory terminal for the synaptic weight, can emulate the pupillary reflex in response to external light stimuli, as illustrated in Figure 5e. Here, an EPSC of 10 nA is set as the response threshold that induces discomfort in the human eye. The EPSC remains below the threshold when the device is exposed to a moderate illuminated environment (365 nm, 7 μW/cm^2). However, exposure to strong light illumination (365 nm, 14 μW/cm^2) results in an EPSC that exceeds the threshold. When a gate bias of −1.5 V is simultaneously applied to the device, the EPSC of the device exposed to a strong light stimulus falls below the threshold, simulating the pupillary contraction response in biological neural systems. This phenomenon may occur due to the negative gate bias, which reduces the initial concentration of channel electrons. This reduction subsequently leads to a decrease in the incremental ratio of photoinduced additional carriers, ultimately resulting in a diminished amplitude of the EPSC. Additionally, the application of a negative gate voltage induces upward band bending in the IGZO channel, which subsequently raises the ionization barrier of V_O. This enhanced barrier necessitates that oxygen vacancies absorb greater energy to facilitate electron release into the conduction band, thereby further constraining the enhancement of the electric field-induced photocurrent (EPSC).[47] Thus, the pupillary reflex can be achieved in our designed transistor by integrating both electrical and optical plasticity, highlighting the advantage of a dual-mode operation for artificial vision applications.

4. CONCLUSIONS

In summary, we propose an IGZO optoelectronic synaptic transistor utilizing an all-solid-state Li-ZrO_2 electrolyte as a gate dielectric layer. The transistor could be successfully prepared using an all-solution method. The designed transistor enables dual-mode electric and optical synaptic plasticity. The electric synaptic plasticity and tunable conductance observed can be attributed to electrochemical doping at the Li-ZrO_2/IGZO interface induced by electrical stimuli. Based on the electric potentiation and depression process, a CNN was designed to classify handwritten digits from the MNIST data set, achieving an accuracy of 96.8%. The transistor exhibits diverse optical synaptic plasticity responses to light illumination, such as PIDP, PWDP, PFDP, PNDP, and PPF, demonstrating the potential of neuromorphic sensing. Finally, sophisticated neuromorphic applications, including logic operations, Pavlov's classical conditioned reflex, and pupillary reflex, have been demonstrated. This work introduces a facile and valuable method for the development of dual-mode optoelectronic synaptic transistors, which possess considerable potential for future neuromorphic vision applications.

■ ASSOCIATED CONTENT

Supporting Information

The Supporting Information is available free of charge at https://pubs.acs.org/doi/10.1021/acsomega.5c01052.

Figure S1. Optoelectronic synaptic device testing schematic. Figure S2: Cross-sectional SEM image of a Li-ZrO_2 layer. Figure S3: Transfer curve for the device without Li^+ doping. Figure S4. Schematic diagram of the doping/dedoping mechanism of conducting ions. Figure S5: Transfer characteristics of the device with Li-ZrO_2 layers annealed at different temperatures. Figure S6: The potentiation and depression processes by UV light pulses and negative gate voltage pulses. Figure S7: The minimum energy consumption for a single synaptic activity of the device. Figure S8. Schematic illustration of the sub-bandgap photon-induced photoresponse mechanism in IGZO (PDF)

■ AUTHOR INFORMATION

Corresponding Author

Shiwei Lin − *State Key Laboratory of Marine Resource Utilization in South China Sea, School of Materials Science and Engineering, Hainan University, Haikou 570228, P. R. China;* orcid.org/0000-0001-7325-8182; Email: linsw@hainanu.edu.cn

Authors

Haonan Xu − *State Key Laboratory of Marine Resource Utilization in South China Sea, School of Materials Science and Engineering, Hainan University, Haikou 570228, P. R. China*

Lilan Zou − *State Key Laboratory of Marine Resource Utilization in South China Sea, School of Materials Science and Engineering, Hainan University, Haikou 570228, P. R. China*

Junru An − *State Key Laboratory of Marine Resource Utilization in South China Sea, School of Materials Science and Engineering, Hainan University, Haikou 570228, P. R. China*

Complete contact information is available at: https://pubs.acs.org/10.1021/acsomega.5c01052

Author Contributions

‡H.X. and L.Z. contributed equally to this work.

Notes

The authors declare no competing financial interest.

■ ACKNOWLEDGMENTS

This work was supported by the National Natural Science Foundation of China (grant nos. U23A20292 and 52162025), the Collaborative Innovation Center Project of Hainan University (XTCX2022XXB01), and the specific fund of the Innovation Platform for Academicians of Hainan Province. Figure 1a was drawn using pictures from Servier Medical Art. Servier Medical Art, by Servier, licensed under a Creative Commons Attribution 3.0 Unported License (https://creativecommons.org/licences/by/3.0/).

■ REFERENCES

(1) Shao, H.; Li, Y.; Yang, W.; He, X.; Wang, L.; Fu, J.; Fu, M.; Ling, H.; Gkoupidenis, P.; Yan, F.; Xie, L.; Huang, W. A Reconfigurable Optoelectronic Synaptic Transistor with Stable Zr-$CsPbI_3$ Nanocrystals for Visuomorphic Computing. *Adv. Mater.* **2023**, *35* (12), No. 2208497.

(2) Yang, R.; Tian, Y.; Hu, L.; Li, S.; Wang, F.; Hu, D.; Chen, Q.; Pi, X.; Lu, J.; Zhuge, F.; Ye, Z. Dual-input optoelectronic synaptic transistor based on amorphous ZnAlSnO for multi-target neuromorphic simulation. *Mater. Today Nano* **2024**, *26*, No. 100480.

(3) Sui, N.; Ji, Y.; Li, M.; Zheng, F.; Shao, S.; Li, J.; Liu, Z.; Wu, J.; Zhao, J.; Li, L. Photoprogrammed Multifunctional Optoelectronic Synaptic Transistor Arrays Based on Photosensitive Polymer-Sorted Semiconducting Single-Walled Carbon Nanotubes for Image Recognition. *Adv. Sci.* **2024**, *11* (29), No. 2401794.

(4) Liu, Z.; Fang, Y.; Cai, Z.; Liu, Y.; Dong, Z.; Zheng, R. X.; Shen, Z.; Wu, R.; Qu, W. J.; Fu, J.; Ru, C.; Wu, Y.; Gu, J.; Liu, Y.; Liu, Q.; Zhao, C.; Wen, Z. Advanced dual-input artificial optical synapse for recognition and generative neural network. *Nano Energy* **2024**, *132*, No. 110347.

(5) Zhang, H.; Liang, F.; Yang, L.; Gao, Z.; Liang, K.; Liu, S.; Ye, Y.; Yu, H.; Chen, W.; Kang, Y.; Sun, H. Superior AlGaN/GaN-Based Phototransistors and Arrays with Reconfigurable Triple-Mode Functionalities Enabled by Voltage-Programmed Two-Dimensional Electron Gas for High-Quality Imaging. *Adv. Mater.* **2024**, *36* (36), No. 2405874.

(6) Choi, C.; Leem, J.; Kim, M.; Taqieddin, A.; Cho, C.; Cho, K. W.; Lee, G. J.; Seung, H.; Bae, H. J.; Song, Y. M.; Hyeon, T.; Aluru, N. R.; Nam, S.; Kim, D. H. Curved neuromorphic image sensor array using a MoS_2-organic heterostructure inspired by the human visual recognition system. *Nat. Commun.* **2020**, *11* (1), 5934.

(7) Yang, Z.; Zhang, T.; Liu, K.; Dang, B.; Xu, L.; Yang, Y.; Huang, R. Neuromorphic Artificial Vision Systems Based on Reconfigurable Ion-Modulated Memtransistors. *Adv. Intell. Syst.* **2023**, *5* (8), No. 2300026.

(8) Li, Z.; Li, M.; Zhu, T.; Li, B.; Wang, Z.; Shao, S.; Deng, Z.; Zhao, X.; Liu, C.; Zhao, J. Flexible Printed Ultraviolet-to-Near-Infrared Broadband Optoelectronic Carbon Nanotube Synaptic Transistors for Fast and Energy-Efficient Neuromorphic Vision Systems. *Small Methods* **2024**, *8* (12), No. 2400359.

(9) Shan, X.; Zhao, C.; Lin, Y.; Liu, J.; Zhang, X.; Tao, Y.; Wang, C.; Zhao, X.; Wang, Z.; Xu, H.; Liu, Y. Optoelectronic synaptic device based on ZnO/HfO_x heterojunction for high-performance neuromorphic vision system. *Appl. Phys. Lett.* **2022**, *121* (26), No. 263501.

(10) Dai, S.; Zhao, Y.; Wang, Y.; Zhang, J.; Fang, L.; Jin, S.; Shao, Y.; Huang, J. Recent Advances in Transistor-Based Artificial Synapses. *Adv. Funct. Mater.* **2019**, *29* (42), No. 1903700.

(11) Lin, J.; Li, B.; Yin, Z.; Wan, S.; Meng, Y.; Zhou, H.; Gao, F.; Li, S.; Zhang, Y.; Zha, Q.; Li, J.; Khisro, S. N.; Chen, X. Optoelectronic synapse based on the $Bi_2O_2Se/Cs_3Cu_2I_5$ heterojunction for neuromorphic computing. *Appl. Phys. Lett.* **2025**, *126* (1), No. 013502.

(12) Su, Z.; Yan, Y.; Sun, M.; Xuan, Z.; Cheng, H.; Luo, D.; Gao, Z.; Yu, H.; Zhang, H.; Zuo, C.; Sun, H. Broadband Artificial Tetrachromatic Synaptic Devices Composed of 2D/3D Integrated WSe_2-GaN-based Dual-Channel Floating Gate Transistors. *Adv. Funct Mater.* **2024**, *34* (33), No. 2316802.

(13) Nguyen, N.; Schneegans, O.; Salot, R.; Lamy, Y.; Giapintzakis, J.; Mai, V. H.; Oukassi, S. An Ultralow Power Li_xTiO_2 -Based Synaptic Transistor for Scalable Neuromorphic Computing. *Adv. Electron Mater.* **2022**, *8* (12), No. 2200607.

(14) Zhu, L.; Gao, H. Z.; Xu, W. R.; Wang, J. M.; Li, W.; Jiang, X. D. Optoelectronic artificial synapse based on $Si_{1-x}Sn_x$ alloyed film. *Vacuum* **2023**, *212*, No. 112002.

(15) Li, J.; Jiang, D.; Yang, Y.; Zhou, Y.; Chen, Q.; Zhang, J. Li-Ion Doping as a Strategy to Modulate the Electrical-Double-Layer for Improved Memory and Learning Behavior of Synapse Transistor Based on Fully Aqueous-Solution-Processed In_2O_3/AlLiO Film. *Adv. Electron Mater.* **2020**, *6* (4), No. 1901363.

(16) Yang, C.; Shang, D.; Liu, N.; Fuller, E. J.; Agrawal, S.; Talin, A. A.; Li, Y.; Shen, B.; Sun, Y. All-Solid-State Synaptic Transistor with Ultralow Conductance for Neuromorphic Computing. *Adv. Funct. Mater.* **2018**, *28* (42), No. 1804170.

(17) Jiang, D.; Li, J.; Fu, W.; Chen, Q.; Yang, Y.; Zhou, Y.; Zhang, J. Light-Stimulated Artificial Synapse with Memory and Learning Functions by Utilizing an Aqueous Solution-Processed In_2O_3/AlLiO Thin-Film Transistor. *ACS Appl. Electron. Mater.* **2020**, *2* (9), 2772−2779.

(18) He, B.; He, G.; Hu, Q.; Jiang, S.; Gao, Q.; Fortunato, E.; Martins, R. Electrospinning-Driven Binary Oxide Nanofiber Networks with Tunable Amorphous Microstructure for Booming Transistors and Circuits Operation. *Adv. Funct. Mater.* **2023**, *9* (5), No. 2300032.

(19) Jeong, J. H.; Ma, J. H.; Park, M. H.; Ha, H. J.; Kang, S. J.; Yun, J. M.; Kim, Y. b.; Kim, E.; Kang, S. J. Oxide Based Pentachromatic-Vision Inspired Optoelectronic Synaptic Transistor with Large Conduction States Over 512. *Adv. Funct. Mater.* **2024**, *34* (38), No. 2402222.

(20) Liu, X.; Wang, D.; Chen, W.; Kang, Y.; Fang, S.; Luo, Y.; Luo, D.; Yu, H.; Zhang, H.; Liang, K.; Fu, L.; Ooi, B. S.; Liu, S.; Sun, H. Optoelectronic synapses with chemical-electric behaviors in gallium nitride semiconductors for biorealistic neuromorphic functionality. *Nat. Commun.* **2024**, *15* (1), 7671.

(21) Zhu, Y.; Peng, B.; Zhu, L.; Chen, C.; Wang, X.; Mao, H.; Zhu, Y.; Fu, C.; Ke, S.; Wan, C.; Wan, Q. IGZO nanofiber photoelectric neuromorphic transistors with indium ratio tuned synaptic plasticity. *Appl. Phys. Lett.* **2022**, *121* (13), No. 133502.

(22) Zhang, J.; Guo, P.; Guo, Z.; Li, L.; Sun, T.; Liu, D.; Tian, L.; Zu, G.; Xiong, L.; Zhang, J.; Huang, J. Retina-Inspired Artificial Synapses with Ultraviolet to Near-Infrared Broadband Responses for Energy-Efficient Neuromorphic Visual Systems. *Adv. Funct. Mater.* **2023**, *33* (32), No. 2302885.

(23) Wang, Y.; Zhou, R.; Cong, H.; Chen, G.; Ma, Y.; Xin, S.; Ge, D.; Qin, Y.; Ramakrishna, S.; Liu, X.; Wang, F. Weak UV-Stimulated Synaptic Transistors Based on Precise Tuning of Gallium-Doped Indium Zinc Oxide Nanofibers. *Adv. Fiber Mater.* **2023**, *5* (6), 1919−1933.

(24) Jiang, Z.; Wen, W.; Zhong, Z.; Xia, L.; Gao, F.; Zhang, Y.; Wu, J.; Khisro, S. N.; Zha, A.; Zha, Q.; Chen, X. Equalizing Excitation-Inhibition via the Ambipolar Photoresponse of Al_2O_3/graphene Hybrid Neuromorphic Devices. *Adv. Electron Mater.* **2022**, *8* (9), No. 2200319.

(25) Park, J.; Jang, Y.; Lee, J.; An, S.; Mok, J.; Lee, S. Synaptic Transistor Based on In-Ga-Zn-O Channel and Trap Layers with Highly Linear Conductance Modulation for Neuromorphic Computing. *Adv. Electron Mater.* **2023**, *9* (6), No. 2201306.

(26) Han, H.; Yu, H.; Wei, H.; Gong, J.; Xu, W. Recent Progress in Three-Terminal Artificial Synapses: From Device to System. *Small* **2019**, *15* (32), No. 1900695.

(27) Park, H.; Oh, S.; Jeong, S. H.; Kwon, O.; Seo, H. Y.; Kwon, J. D.; Kim, Y.; Park, W.; Cho, B. Dual-Terminal Stimulated Heterosynaptic Plasticity of IGZO Memtransistor with Al_2O_3/TiO_2 Double-Oxide Structure. *ACS Appl. Mater. Interfaces* **2022**, *4* (6), 2923−2932.

https://doi.org/10.1021/acsomega.5c01052
ACS Omega 2025, 10, 16884−16891

(28) Jang, H. Y.; Kwon, O.; Nam, J. H.; Kwon, J. D.; Kim, Y.; Park, W.; Cho, B. Highly Reproducible Heterosynaptic Plasticity Enabled by MoS_2/ZrO_{2-x} Heterostructure Memtransistor. *ACS Appl. Mater. Interfaces* **2022**, *14* (46), 52173−52181.
(29) Awan, S. U.; Hasanain, S. K.; Bertino, M. F.; Jaffari, G. H. Effects of substitutional Li on the ferromagnetic response of Li co-doped ZnO:Co nanoparticles. *J. Phys.: Condens. Matter* **2013**, *25* (15), No. 156005.
(30) Liu, Z.; Wang, K.; Jiang, X.; Javed, M. S.; Han, W. Overcoming current leaks in CNT/PDMS triboelectric composites by wrapping CNTs with TiO_2 insulation layer. *Appl. Phys. Lett.* **2022**, *121* (11), No. 113505.
(31) Chen, B.; Sun, S.; Fan, S.; Liu, X.; Li, Q.; Su, J. Low-Cost Fabricated MgSnO Electrolyte-Gated Synaptic Transistor with Dual Modulation of Excitation and Inhibition. *Adv. Electron Mater.* **2022**, *8* (12), No. 2200864.
(32) Miao, G.; Liu, Q.; Shi, Y.; Ci, R.; Liu, G.; Shan, F. Artificial synapses based on boron ions-modulated transistors for neuromorphic applications. *Appl. Phys. Lett.* **2024**, *124* (20), No. 203301.
(33) Liu, Q.; Yin, L.; Zhao, C.; Wu, Z.; Wang, J.; Yu, X.; Wang, Z.; Wei, W.; Liu, Y.; Mitrovic, I. Z.; Yang, L.; Lim, E. G.; Zhao, C. Z. All-in-one metal-oxide heterojunction artificial synapses for visual sensory and neuromorphic computing systems. *Nano Energy* **2022**, *97*, No. 107171.
(34) Lecun, Y.; Bottou, L.; Bengio, Y.; Haffner, P. Gradient-based learning applied to document recognition. *Proc. IEEE* **1998**, *86* (11), 2278−2324.
(35) Yang, R.; Yin, L.; Lu, J.; Lu, B.; Pi, X.; Li, S.; Zhuge, F.; Lu, Y.; Shao, W.; Ye, Z. Optoelectronic Artificial Synaptic Device Based on Amorphous InAlZnO Films for Learning Simulations. *ACS Appl. Mater. Interfaces* **2022**, *14* (41), 46866−46875.
(36) Ke, S.; Fu, C.; Lin, X.; Zhu, Y.; Mao, H.; Zhu, L.; Wang, X.; Chen, C.; Wan, C.; Wan, Q. BCM Learning Rules Emulated by a-IGZO-Based Photoelectronic Neuromorphic Transistors. *IEEE Trans. Electron Devices* **2022**, *69* (8), 4646−4650.
(37) Lim, T.; Lee, J.; Woo, D. Y.; Kwak, J. Y.; Jang, J. Multifunctional Crystalline InGaSnO Phototransistor Exhibiting Photosensing and Photosynaptic Behavior Using Oxygen Vacancy Engineering. *Small Methods* **2023**, *7* (9), No. 2300251.
(38) Lee, M.; Lee, W.; Choi, S.; Jo, J.; Kim, J.; Park, S. K.; Kim, Y. Brain-Inspired Photonic Neuromorphic Devices using Photodynamic Amorphous Oxide Semiconductors and their Persistent Photoconductivity. *Adv. Mater.* **2017**, *29* (28), No. 1700951.
(39) Kim, M.; Lee, J. Synergistic Improvement of Long-Term Plasticity in Photonic Synapses Using Ferroelectric Polarization in Hafnia-Based Oxide-Semiconductor Transistors. *Adv. Mater.* **2020**, *32* (12), No. 1907826.
(40) Zhang, J.; Shi, Q.; Wang, R.; Zhang, X.; Li, L.; Zhang, J.; Tian, L.; Xiong, L.; Huang, J. Spectrum-dependent photonic synapses based on 2D imine polymers forpower-efficient neuromorphic computing. *InfoMat* **2021**, *3* (8), 904−916.
(41) Zhou, J.; Li, H.; Tian, M.; Chen, A.; Chen, L.; Pu, D.; Hu, J.; Cao, J.; Li, L.; Xu, X.; Tian, F.; Malik, M.; Xu, Y.; Wan, N.; Zhao, Y.; Yu, B. Multi-Stimuli-Responsive Synapse Based on Vertical van der Waals Heterostructures. *ACS Appl. Mater. Interfaces* **2022**, *14* (31), 35917−35926.
(42) Tan, H.; Liu, G.; Yang, H.; Yi, X.; Pan, L.; Shang, J.; Long, S.; Liu, M.; Wu, Y.; Li, R. W. Light-Gated Memristor with Integrated Logic and Memory Functions. *ACS Nano* **2017**, *11* (11), 11298−11305.
(43) Lin, Y.; Meng, F.; Zeng, T.; Zhang, Q.; Wang, Z.; Cheng, Y.; Zhao, X.; Gu, L.; Xu, H.; Liu, Y. Direct Observation of Oxygen Ion Dynamics in a WO_{3-x} based Second-Order Memristor with Dendritic Integration Functions. *Adv. Funct. Mater.* **2023**, *33* (35), No. 2302787.
(44) Shrivastava, S.; Keong, L. B.; Pratik, S.; Lin, A. S.; Tseng, T. Fully Photon Controlled Synaptic Memristor for Neuro-Inspired Computing. *Adv. Electron Mater.* **2023**, *9* (3), No. 2201093.
(45) Li, Q.; Wang, T.; Fang, Y.; Hu, X.; Tang, C.; Wu, X.; Zhu, H.; Ji, L.; Sun, Q. Q.; Zhang, D. W.; Chen, L. Ultralow Power Wearable Organic Ferroelectric Device for Optoelectronic Neuromorphic Computing. *Nano Lett.* **2022**, *22* (15), 6435−6443.
(46) Meng, J.; Wang, T.; Zhu, H.; Ji, L.; Bao, W.; Zhou, P.; Chen, L.; Sun, Q. Q.; Zhang, D. W. Integrated In-Sensor Computing Optoelectronic Device for Environment-Adaptable Artificial Retina Perception Application. *Nano Lett.* **2022**, *22* (1), 81−89.
(47) Liu, Q.; Yin, L.; Zhao, C.; Wang, J.; Wu, Z.; Lei, H.; Liu, Y.; Tian, B.; Zhang, Z.; Zhao, Z.; Liu, R.; Ding, C.; Han, Y.; Ma, C. Q.; Song, P.; Mitrovic, I. Z.; Lim, E. G.; Wen, Z. Hybrid Mixed-Dimensional Perovskite/Metal-Oxide Heterojunction for All-in-One Opto-electric Artificial Synapse and Retinal-Neuromorphic System. *Nano Energy* **2022**, *102*, No. 107686.

https://doi.org/10.1021/acsomega.5c01052
ACS Omega 2025, 10, 16884−16891